Int J Thermophys (2009) 30:1283–1299
DOI 10.1007/s10765-009-0597-z

A Numerical Simulation to Propose a Flash Method for In Situ Detection of the Thermal Diffusivity of Anisotropic Thin Film Materials

Oleg Yu. Troitsky · Harald Reiss

Received: 10 November 2008 / Accepted: 13 May 2009 / Published online: 2 June 2009

Abstract Strong anisotropy of thermal diffusivity is frequently observed in thin film materials. We propose an in situ experimental method to remotely measure radial and axial components of the thermal diffusivity. The method is based on the traditional laser flash technique but is specialized to also highly challenging experimental situations such as sample manufacture and use phase when thin films may be exposed to very high pressures or temperatures and to high temperature gradients. The method requires laser pulses of very short duration and fast measurement of transient temperature excursions in only radial directions on the surface of the thin film samples. The accuracy of the method is checked by comparison with results from a finite element calculation for a graphite sheet with high anisotropic conductivity that simulates a thermo-physical experiment.

Keywords Anisotropy · Flash method · Thermal diffusivity · Thin films

List of symbols

- a Thermal diffusivity, $m^2 \cdot s^{-1}$
- b Sample thickness, m
- c Specific heat, $J \cdot kg^{-1} \cdot K^{-1}$
- d Radius of target spot, m
- F Quantity defined in Eq. 7b

O. Y. Troitsky
Department of Applied Computer Science, Seversk State Technology Academy,
65 Kommunisticheskiy Avenue, Seversk, Tomsk Region 636036, Russia

H. Reiss (✉)
Department of Physics, University of Würzburg, Am Hubland, 97074 Würzburg, Germany
e-mail: harald.reiss@physik.uni-wuerzburg.de

Fo Fourier number
i Node number in numerical simulation
Q Heat pulse, J
r Radial coordinate, m
r_i Radial coordinate of node i, m
R Radius of thin film sample or sheet, m
t Time, s
t_A Time at a reference point A, s
T Temperature, K
T_0 Thermal homogeneity criterion, compare Eq. 1
T' Derivative of temperature with time, $\mathrm{K} \cdot \mathrm{s}^{-1}$
x Vertical coordinate, m
Bi Biot number

Greek

λ Thermal conductivity, $\mathrm{W} \cdot \mathrm{m}^{-1} \cdot \mathrm{K}^{-1}$
ρ Density, $\mathrm{kg} \cdot \mathrm{m}^{-3}$
σ Stefan–Boltzmann constant, $5.667 \times 10^{-8}\ \mathrm{W} \cdot \mathrm{m}^{-2} \cdot \mathrm{K}^{-4}$
θ Dimensionless temperature
α Heat transfer coefficient, $\mathrm{W} \cdot \mathrm{m}^{-2} \cdot \mathrm{K}^{-1}$

1 Introduction

Intensive heat and mass transfer is involved in the manufacture of power electronic devices during evaporation of thin films or in diffusion processes, or of thermal shields for gas turbines during plasma spraying, or when preparing protective layers by chemical vapour deposition (CVD) on aerospace and atomic energy installations. Moreover, in their use phase, thin film materials may be subject to very high pressures or temperatures and to high temperature gradients. Accordingly, there is a clear need for accurate determination of thermal diffusivity under in situ conditions, not only during preparation but also if anisotropy of thermo-physical properties arises during ageing of the films.

The thermal wave technique is frequently used for measurements of the thermal diffusivity of thin films including investigation of sub-surface structures such as detection of cracks and other disturbances that may arise during manufacture or result from materials fatigue during the use phase. This technique comprises scanning photo-acoustic microscopy, the mirage effect, infrared radiometry, or measurement of optical displacement (see, e.g., [1] for a survey, and the literature cited therein). Thermal waves are generated from localized heat sources created under an intensity-modulated laser or electron beam irradiation; the thermo-reflectance microscope (compare, e.g., [2]) operates with even point-like heat sources. By variation of the modulation frequency, surface or in-depth scanning of the thermal transport properties including interfacial resistances of layered samples can be performed.

In the present state of the art, these methods work successfully under the following conditions:

(a) stationary "background" sample temperature,
(b) isotropic properties of the samples to be investigated,
(c) opacity of sample or substrate material, and
(d) laboratory conditions, such as in the thermo-reflectance microscope

However, condition (a) may not be fulfilled during sample manufacture and use phases. It is even questionable whether the time interval, Δt, needed to reach stationary thermal wave propagation is short enough to avoid collisions with "internal" variations of sample properties (temperature or sample thickness). Not all thin film deposition methods operate under stationary conditions. For example, plasma spraying of a protective coating on a turbine blade is performed by running the beam (droplets of molten metallic or ceramic powder delivered by a spray gun) line by line over the substrate. This induces strong variations, with a frequency on the order of seconds, of sample temperature during growth of the coating. The interval, Δt, scales with L^2/a and is nearly independent of frequency (compare the solution found by Drach [3] using a Laplace transform of the heat conduction equation), with L, the thickness of the coating and a, its diffusivity. In case the diffusivity is small, this means Δt too, can extend to several seconds so that the intensity-modulated thermal wave experiment cannot follow variations of sample properties quickly enough during deposition.
Condition (b) can rigorously be fulfilled only with polycrystalline thin films, or exceptionally with epitaxially grown films on appropriate substrates, or with pure metals if the film thickness is sufficiently large. Condition (c) is usually applied to the wavelength of the incoming laser radiation, but thin films may be transparent at other wavelengths of the thermal radiation spectrum that inevitably is generated by a heated target area. It is, therefore, questionable whether the transport properties of thin film samples reduce to purely conductive heat flow in case the film is opaque at just the incident laser radiation. Laboratory conditions (d) can hardly be realized if the sample is integrated in a running industrial process, or if the thin film shall be investigated during its preparation, which similar to plasma spraying or CVD, mostly proceed at high temperatures and in closed deposition chambers.
Low-frequency measurements, compare, e.g., Pelzl et al. [4], indicate stronger lateral (parallel to surface) thermal wave propagation, but separation between lateral and normal directions by frequency variation at best delivers an approach that would be justified only if lateral thermal diffusivity and effusivity are much larger than the corresponding normal components.
Alternatively, 3ω ([5,6]) and hot-strip methods [7] are candidates for measuring the thermal conductivity of thin films. Instead of an irradiated target spot, both methods apply heated metallic strips as heat sources prepared on the sample; the strips also serve as resistance thermometers to detect temperature variations on the sample surface. Both methods suffer at least from problems (a) and (d), as before. However, using the 3ω method, anisotropic transport properties even of superconducting thin films at cryogenic temperature have been determined ([6]), such as the properties of BiSrCaCuO powder in tube conductors, with an anisotropy ratio of the thermal conductivity on the order of 10 to 100, between c- and ab-axis orientation.

In this article, we propose another flash method to cover not only the field of anisotropic thin films but also *remote* investigation of their in situ properties during deposition or industrial application.

Contrary to intensity-modulated measurements, we do not have the problem associated with time interval, Δt, needed to obtain quasi-stationary thermal wave propagation before data may be taken: A laser pulse can be made short enough not to collide with transient temperature excursions in a thin film during deposition. Data collection may be started immediately after the end of the pulse. However, the question is whether also the temperature *excursion* generated by the laser pulse will not collide with internal variation of the sample temperature (that, as before, may arise in a fast or oscillating deposition process or under transient load conditions). As will be shown in Sect. 3 for a graphite thin film, extraction of its axial and radial diffusivity components can be realized using data (temperature excursion on the sample front side) taken already after 400 ms or between 35 ms and 55 ms, respectively, after deposition of the laser pulse. The proposed method also applies rather simple analytical expressions.

While remote measurements of thermal diffusivity have been discussed extensively in the literature, the traditional laser flash technique is not sufficiently advanced for anisotropic materials. Although Taguchi and Nagasaka [8] extended the theory of two-dimensional heat conduction and verified the capability of dynamic grating radiometry to investigate anisotropic materials, their experimental assembly is too complex for in situ measurements.

We previously introduced a new front-face flash-monitoring method [9] for remote investigation of two-layer thin-film samples of *isotropic* thermal conductivity. Instead of taking temperatures directly at the pulsed heating region, we suggested in [10] to measure temperature at *any* distance from the center of the heating spot (in this respect, the flash method is similar to photothermal displacement studies by Fournier et al. [2] and Pelzl et al. [4]). The method does not need corrections to radiative and convective heat losses, and it also avoids the serious limitations suffered by standard methods when samples are *transparent* or *semi-transparent;* this means that problem (c) mentioned above can be avoided. The results also do not depend on sample thickness. Simultaneous remote measurement of the diffusivity and absorption coefficient of thin film, isotropic materials was introduced in [11].

In this article, we describe application of a remote method to an anisotropic material and an investigation whether different temporal or spatial distributions of laser power may affect results for radial and axial diffusivity components. Moreover, this article applies photothermal displacement but the advantage of the displacement becomes clear especially under industrial working conditions when some positions of the target spot might not be visible for a Thermo-Vision system. A graphite sheet with high anisotropy in directions parallel and perpendicular to the irradiated plane is taken as an example.

For proper use of the analytical expressions presented in [9–11] and in this article, the dimensionless criterion of thermal homogeneity,

$$T_0(t) = [T(t)/t]/[\mathrm{d}T(t)/\mathrm{d}t] \tag{1}$$

identifies the region of Fourier numbers, *Fo*, where the heating regime is regular and the analytical solutions may be applied to measured temperature excursions, $T(t)$. Behaviour of T_0, as a function of Fourier number, has been discussed in [9] for different experimental conditions.

2 Description of the Method

2.1 Equation of Heat Conduction in Cylindrical Coordinates

Radial and axial coordinates and dimensions of a thin film sample are illustrated in Fig. 1. The sample is irradiated by an axially symmetric laser beam of uniform intensity delivering a short (rectangular) heat pulse to a cylindrical target spot located at $x = 0$ with dimensions $0 \leq r \leq d$ (non-uniform, temporal, or spatial laser beam intensity will be discussed in Sect. 3.3). Transient temperature excursion is measured at the center of the specimen ($x = 0, r = 0$) and at positions r_i ($x = 0, d < r_i < R$) outside the target spot (the index i denotes position number).
If the thermal diffusivity components are independent of temperature, the heat conduction in anisotropic materials, without convective or radiative losses to the ambient, is described by

$$\alpha_r \frac{\partial^2 \theta}{\partial r^2} + \frac{\alpha_r}{r} \frac{\partial \theta}{\partial r} + \alpha_x \frac{\partial^2 \theta}{\partial x^2} = \frac{\partial \theta}{\partial t} \tag{2}$$

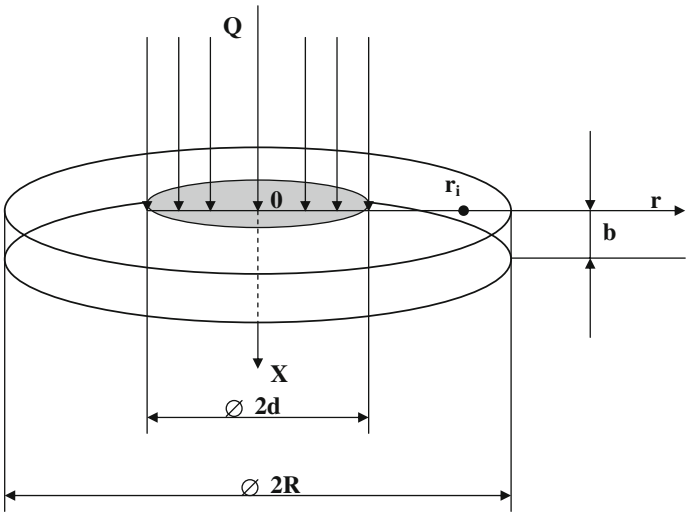

Fig. 1 Transient heat conduction (schematic) in a disk of thickness, b, and radius, R. The target spot of radius d is irradiated at $x = 0$. Nodes with radial distance, r_i, from the center of the sample ($x = 0, r = 0$) will be applied in the numerical simulation, compare with text

In Eq. 2, $\theta(t)$ denotes the (dimensionless) temperature excursion with time, t, r is the radius, x is the distance into the sample of thickness, b, and a_r and a_x indicate the corresponding thermal-diffusivity components.
Boundary condition at $t = 0$ is

$$\theta(x,r,0) = \begin{cases} \frac{Q}{c\rho g} & \text{for } x = 0,\ 0 \le r \le d \\ 0 & \text{for } x = 0,\ d < r \le R \\ 0 & \text{for } 0 < x \le b,\ 0 \le r \le R \end{cases} \tag{3}$$

and for $t > 0$

$$\left.\frac{\partial\theta(x,r,t)}{\partial x}\right|_{\substack{x=0\\x=b}} = \left.\frac{\partial\theta(x,r,t)}{\partial r}\right|_{r=R} = 0 \tag{4}$$

under adiabatic conditions. In Eq. 3, Q denotes the heat pulse, ρ is the density of the thin film material, c is its specific heat, and g is the depth of energy absorption.

2.2 Separation into Axial and Radial Diffusivity Components

For determination of a temperature excursion with time in a conductive solid, Carslaw and Jaeger [12, pp. 256, 356] showed that an initial temperature distribution is equivalent to a distribution of instantaneous, initial heat sources. They also showed [12, pp. 33–35] that in certain regular solids (such as orthotropic, as is the case here for strong anisotropy), heat flow components perpendicular to each other can be treated separately. Accordingly, for a right cylinder with an axially symmetrical, initial temperature distribution, or with equivalent instantaneous, initial heat sources, and for strong anisotropic conductivity, Eq. 2 can be split into axial and radial components:
For the axial component, $\theta(x,t)(t > 0, 0 < x < b)$, we have

$$\frac{\partial\theta}{\partial t} = \alpha_x \frac{\partial^2\theta}{\partial x^2} \tag{5}$$

and for the radial component $\theta(r,t)(t > 0, 0 < r < R)$

$$\frac{\partial\theta}{\partial t} = \alpha_r \frac{\partial^2\theta}{\partial r^2} + \alpha_r \frac{1}{r}\frac{\partial\theta}{\partial r} \tag{6}$$

The final result is the product of the corresponding one-variable solutions. Extension to pulses of finite duration may be obtained by integration of the results provided by Eqs. 5 and 6 with respect to time.

2.3 Extraction of Axial and Radial Components of the Diffusivity

Equation 5 for the axial component, a_x, of the diffusivity can be solved analytically, as we have reported previously ([9]);

$$\alpha_x = -\frac{b^2 \ln F}{\pi^2 \Delta\tau} \tag{7a}$$

$$\text{using} \quad F = \frac{\sum_{k=1}^{n} T^k \sum_{k=1}^{n} T^{k-1} - n \sum_{k=1}^{n} T^k T^{k-1}}{(\sum_{k=1}^{n} T^{k-1})^2 - n \sum_{k=1}^{n} (T^{k-1})^2} \tag{7b}$$

In Eq. 7b, T^k denotes temperature measured at time, t_k, at the point $x = 0$, $r = 0$, and n is the number of temperature measurements taken at this position with time steps, $\Delta\tau$, in-between.
Equation 6 for determination of the radial component, a_r, can be replaced by a finite difference relation, and then can be solved yielding

$$\alpha_r = \frac{\frac{T_i^k - T_i^{k-1}}{\Delta t}}{\frac{T_{i+1}^k - T_{i-1}^k}{2 r_i \Delta r} + \frac{T_{i+1}^k - 2T_i^k + T_{i-1}^k}{(\Delta r)^2}} \tag{8}$$

In Eq. 8, T_i^k denotes temperature measured at time, t_k, at position number, i, with $x = 0$, $r = r_i$. The intervals are defined by $\Delta t = t_k - t_{k-1} = t_{k+1} - t_k$, and $\Delta r = r_{i+1} - r_i$.

3 Numerical Simulation of a Thermophysical Experiment

As a test of the proposed method, finite element calculations have been performed to simulate a real thermophysical experiment for determination of axial and radial components of the thermal diffusivity. In a rigorous sense, the proposed analytical tools can be proved only by application of another analytical or by a numerical tool that provides exact solutions. Finite element methods usually are considered as exact in conduction heat transfer. Experiments, on the other hand, suffer from data scattering and thus cannot provide a rigorous (mathematical) confirmation of the expressions; instead, experiments demonstrate *applicability* of a proposed method if the results obtained by the new method agree with already existing data.
In the first step, the numerical simulation yields the excursion with time of the surface temperature, and the dependence of the data input made for irradiation and materials diffusivity. This procedure (calculation of transient surface temperature) simulates a real thermophysical experiment (remote temperature measurement) using any matrix infrared Thermo-Vision system with sufficiently high data collection and handling rates. In the second step, the diffusivity components will be extracted from the simulated temperature excursions using the solutions of Eqs. 7a and 8, and the results in turn compared with the data input into the numerical model.

Assume a solid graphite disk of radius $R = 120$ mm, with sample thickness $b = 1$ mm. The thermal conductivity, λ, of graphite is specified by radial $\lambda_r = 1140\,\mathrm{W\cdot m^{-1}\cdot K^{-1}}$ and axial $\lambda_x = 6.4\,\mathrm{W\cdot m^{-1}\cdot K^{-1}}$ components; specific heat is $c = 623.9\,\mathrm{J\cdot kg^{-1}\cdot K^{-1}}$ and density $\rho = 2260\,\mathrm{kg\cdot m^{-3}}$; the materials properties are from [13, p. 214]. This yields the thermal diffusivity components $a_x = 4.539 \times 10^{-6}\mathrm{m^2\cdot s^{-1}}$ and $a_r = 8.085 \times 10^{-4}\mathrm{m^2\cdot s^{-1}}$, as data input fed into the numerical model.
A laser pulse delivering $Q = 1$ J with a pulse length of 8 ns is used as excitation source and is applied over a heating spot of radius $d = 15$ mm at the front face ($x = 0$) of the sample. Since calculations starts at $T = 0$, all the calculated temperatures, $T(t)$, are over-temperatures.
In order to properly interpret the simulated temperature results, we need reference-time points that can be applied in Eqs. 7a and 8. The criterion T_0, Eq. 1, allows identification of positions, r_i, at which the thermal-diffusivity components versus time may subsequently be determined, see below. The index, i, is taken to also indicate node numbers in the finite element calculations.

3.1 Extraction of the Radial Diffusivity Component

For determination of the radial component, a_r, of the diffusivity, the positions, r_i, should be located clearly *outside* the image of the laser beam (the heated target spot). In the present simulations, they are identified by node numbers 20–25, with radial distances $r_{20} = 18.75$ mm, $r_{21} = 22.5$ mm, $r_{22} = 26.25$ mm, $r_{23} = 30$ mm, $r_{24} = 33.75$ mm, and $r_{25} = 37.5$ mm from the center ($x = 0$, $r = 0$) of the sample. Spacing, 3.75 mm, between these nodes is constant. We will identify these nodes in the following by a "radial node set" $\{N_r\}$. Another set, $\{N_x\}$, will be used for determination of the axial component, a_x, of the diffusivity. The set $\{N_x\}$ comprises the nodes 10–15, all located *inside* the image of the laser beam, with radial distances $r_{10} = 0$ mm, $r_{11} = 1$ mm, $r_{12} = 2$ mm, $r_{13} = 3$ mm, $r_{14} = 4$ mm, and $r_{15} = 15$ mm from the center (node 15 is located on the periphery of the image).
Figure 2 shows results for T_0 using $\{N_r\}$ and the data input for the components a_r and a_x of the diffusivity. Extraction of a_r from the calculated temperatures, $T(t)$, using nodes of the set $\{N_r\}$ by the method described in this article, has to be applied to data points also outside (in time) of the resonance-like oscillations (break points) of T_0 obvious in all the curves plotted in Fig. 2. The oscillations in T_0 can be explained simply from the behavior of $\mathrm{d}T/\mathrm{d}t$ (compare Fig. 3a, b): At any position, r_i, inside or outside the image, $T(t)$ first increases when the laser pulse adiabatically heats the inner nodes, or when the thermal wave arrives at the outer nodes, respectively. Then $T(t)$ runs over a maximum (its width being correlated with conduction properties and thermal capacity of the material) and finally decreases due to conductive losses to positions $r_{i+1} > r_i$. This explains $\mathrm{d}T/\mathrm{d}t$ and T_0. Extraction of the radial diffusivity component yields the results presented in Fig. 4.
For times clearly outside the break points, all the curves in Fig. 4 converge to $a_r = 8.085 \times 10^{-4}\mathrm{m^2\cdot s^{-1}}$, which indicates almost perfect agreement with the input data for the radial diffusivity component used in the numerical simulation.

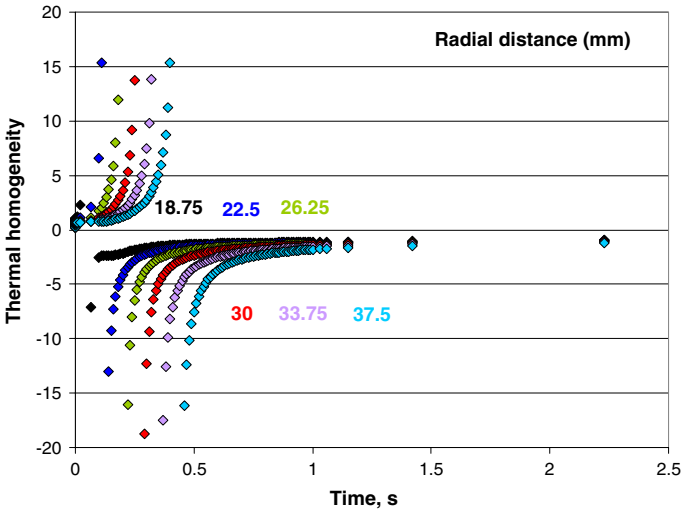

Fig. 2 Criterion of thermal homogeneity, T_0, as a function of time, t, observed at nodes of the set $\{N_r\}$ all the nodes of which are located *outside* the target spot, at different radial distances from the center. The curves result from $T_0 = (T/t)/(\mathrm{d}T/\mathrm{d}t)$, Eq. 1, with temperatures, $T(t)$, obtained in a finite element solution of Eq. 2 with boundary conditions given in Eqs. 3 and 4. Results are given for a graphite sheet subjected to a rectangular laser pulse of homogeneous power density and 8 ns duration; data input is explained in the text. The target spot (image of the laser beam) on the front side of the sample has a radius of 15 mm

It is important that this agreement is demonstrated not only for a single node but for a *distribution* of nodes, here the nodes of the set $\{N_r\}$. As mentioned, in a real thermo-physical experiment and under industrial working conditions, some positions of the target spot might not be visible for a Thermo-Vision system (and also for this reason, a rigorous experimental proof of the suggested methods would not be possible). Determination of the component, a_x, can be made using data obtained rather shortly ($t \geq 400$ ms) after deposition of the laser pulse.

Note that temperature excursions in Fig. 4 are almost identical for the nodes 10–14, for all times 10^{-10} s $\leq t \leq 1$ s. These nodes, all located within the image, experience almost perfect adiabatic conditions during duration of the pulse. At node 15 located at $r = 15$ mm from the center, the temperature is significantly lower, due to conductive heat losses to regions outside the target spot. After $t = 50$ s (end of the simulations), all the curves saturate to $\Delta T = Q/(\rho c V) = 0.0157$ K (over-temperature), with V, the total volume of the disk.

3.2 Extraction of the Axial Component

We must find an interval $0.16 < Fo_x < 0.25$ (compare [14]) in which Eqs. 7a, b may be applied; Fo_x denotes the Fourier number using the axial diffusivity component, a_x, i.e., $Fo_x = a_x t/b^2$. Assume for the moment that a_x is known. The interval $0.16 \leq Fo_x \leq 0.25$ then is uniquely correlated with a time interval $t_1 \leq t \leq t_2$: $Fo_x = 0.16$ yielding the time of regularization, t_1, and $Fo_x = 0.25$ giving t_2, respec-

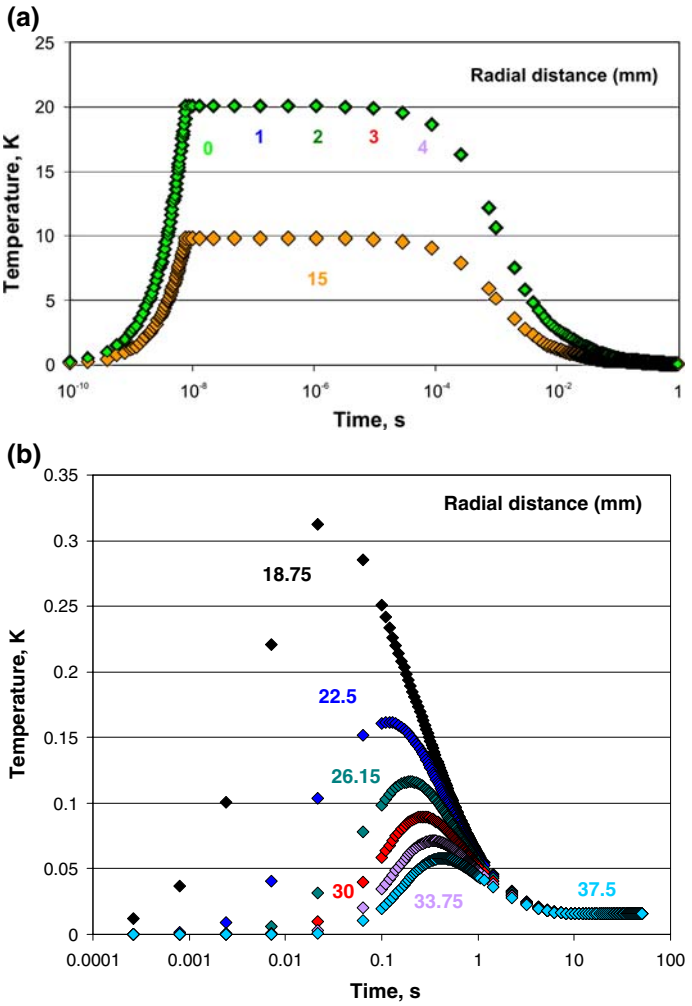

Fig. 3 (**a**) Numerically simulated, transient node temperatures, $T(t)$, obtained in a finite element solution of Eq. 2 with boundary conditions given in Eqs. 3 and 4. Results are given for nodes of the set $\{N_x\}$ all located *inside* the target spot, at different radial distances from the center of the graphite sheet. Results are given for a graphite sheet subjected to a rectangular laser pulse of homogeneous power density and 8 ns duration; data input is explained in the text. The target spot (image of the laser beam) on the front side of the sample has a radius of 15 mm. (**b**) Same plot as in (**a**), but for nodes of the set $\{N_r\}$ all located *outside* the target spot, at different radial distances from the center of the graphite sheet

tively. Application of Eqs. 7a, b at times $t_1 \leq t \leq t_2$ then allows identification of the axial thermal diffusivity from the temperature excursion.

However, the problem is that a_x is unknown. The only available information is provided by measurement of the temperatures, $T(t)$, and the criterion, $T_0(t)$. We accordingly need a calibration that relates T_0 to the Fourier number. This is realized by selection of a reference point, A, in a diagram, T_0 versus t, identifying a reference time, t_A, at

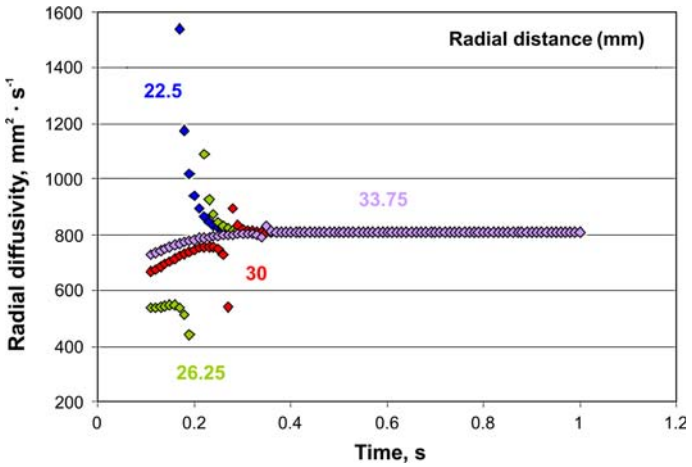

Fig. 4 Radial diffusivity component, a_r, as function of time, t, calculated at nodes of the set $\{N_r\}$; all the nodes are located *outside* the target spot, at different radial distances from the center of the graphite sheet. Data are obtained applying Eq. 8 to numerically simulated, transient node temperatures obtained in a finite element solution of Eq. 2 with boundary conditions given in Eqs. 3 and 4, for the graphite sheet. All the curves converge to the numerical data input, $a_r = 8.085 \times 10^{-4}\,\mathrm{m^2 \cdot s^{-1}}$

which T_0 attains the value $T_0(t = t_A)$. When this time is fixed, a numerical simulation, with diffusivity, a_x, taken as a variable, generates a second diagram, T_0 versus Fo, for constant $t = t_A$. Comparison is made between T_0 in both diagrams. In principle, any of the data points of the curves, T_0, each calculated for the set $\{N_x\}$, can be selected for the reference point, A, but it is convenient to select those positions (in time) where T_0 attains a local maximum or minimum. It is thus clear that the procedure can be applied only to T_0 obtained at positions *inside* the target spot; otherwise, we would again observe resonance-like oscillations similar to those seen in Fig. 2. With $T_0(t = t_A)$ taken from the first diagram, the second diagram allows to identify the Fourier number at which the same value, $T_0(t = t_A)$, is observed.

As in the first diagram, Fig. 5a shows T_0 versus t, using the set $\{N_x\}$. From this set, we first select position (node) number 10, the central node with $r_{10} = 0$, $x = 0$, and for the reference point, A, we select the local minimum of the curve, T_0 versus t, for this node. It is located at $t_A = 13\,\mathrm{ms}$; this yields $T_0(t = t_A) = -1.657$. The local minimum of the $T(t)$ of the other nodes of the set $\{N_x\}$, with non-zero radial distances, is seen at the same t_A, in a good approximation. It is thus sufficient to consider only T_0 of node 10 in the following.

The second diagram, T_0 versus Fo, is given by Fig. 5b. Considering a_x as a variable, the same $T_0(t = t_A) = -1.657$ is attained at $Fo = 0.059 = a_x t_A / b^2$. This immediately determines the diffusivity, a_x (a provisional value, because from a single T_0-curve only) and the interval $t_1 \le t \le t_2$ in which Eqs. 7a, b is valid. Using the provisional a_x, the Fourier numbers $Fo_x = 0.16$ and 0.25 are correlated with $t_1 = 35$ and $t_2 = 55\,\mathrm{ms}$. Application of Eqs. 7a, b to this time interval then allows taking into account all data points taken at times, t, within the interval $t_1 \le t \le t_2$. This finally yields the axial diffusivity component $a_x = 3.800 \times 10^{-6}\,\mathrm{m^2 \cdot s^{-1}}$.

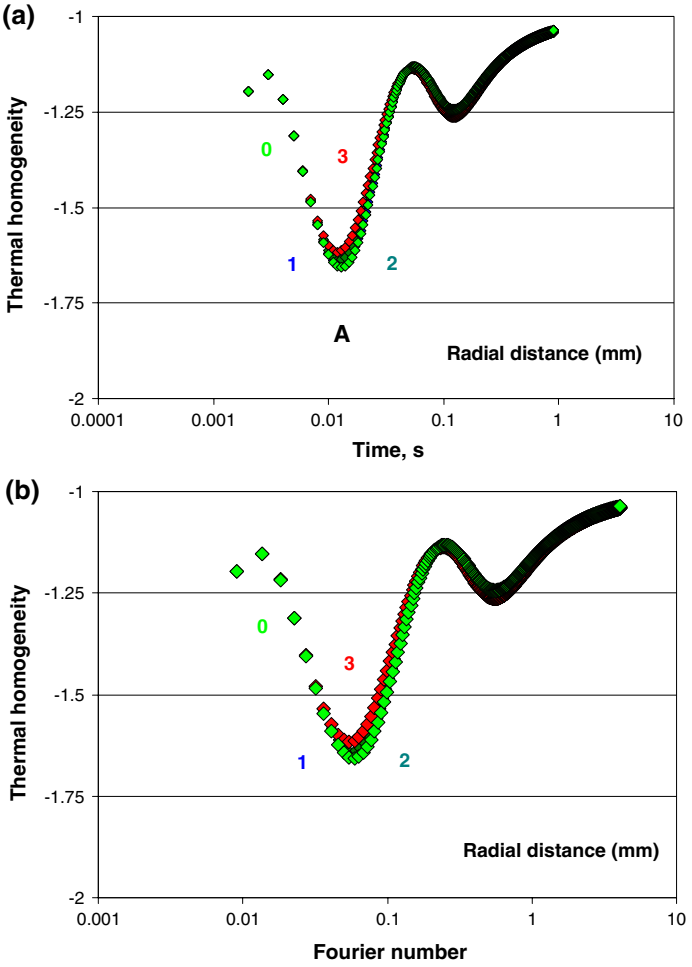

Fig. 5 (**a**) Thermal homogeneity criterion, T_0, calculated at nodes of the set $\{N_x\}$; all nodes are located *inside* the target spot, at different radial distances from the center of the graphite sheet. Time, t_A, is identified from a local minimum of the curves T_0 versus time; this yields $t_A = 13$ ms. (**b**) Thermal homogeneity criterion, T_0, as in (**a**), now plotted versus Fourier number, *Fo*. Compare with text for explaining details of the procedure to extract the axial diffusivity, a_x, from comparison of T_0 in (**a**) and (**b**)

This value is below the original data input for a_x ($4.539 \times 10^{-6}\,\mathrm{m}^2 \cdot \mathrm{s}^{-1}$) by about 15 %. The relatively high discrepancy is due to an assumed low full-frame rate (125 Hz) provided by a standard measuring device like the Thermo-Vision system SC6000 [15]. If used as an experimental instrument, it then would allow a data recording rate of only four experimental points (in the present case, the nodes 10, 11, 12, and 13) in the interval 35 ms $\leq t \leq$ 55 ms. A Thermo-Vision system with higher time resolution and data handling (or, respectively, an extended set $\{N_x\}$, with smaller distances between neighboring nodes) would substantially improve the accuracy: With a full-frame rate of 1000 Hz, the uncertainty will be improved to 2 % or better.

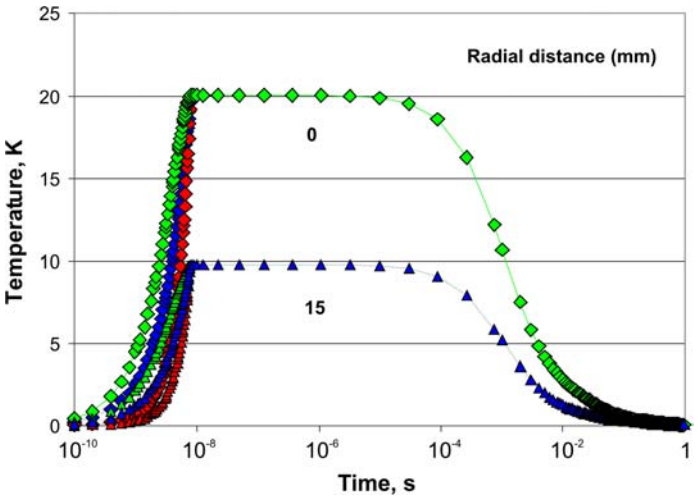

Fig. 6 Numerically simulated, transient node temperatures, $T(t)$, calculated for temporal variations (pulses 1–3) of laser power density impinging on the graphite sheet, with a circular image of 15 mm radius on the front side of the sample. Pulse (1), blue symbols, is rectangular (constant in time), with 1.768×10^{11} W·m^{-2} power density, pulse (2), red symbols, is triangular and increases linearly from zero to maximum value, and pulse (3), green symbols, again triangular, decreases linearly from maximum value to zero. Duration of the pulses 1–3 is 8 ns. Data are given at the center of the laser pulse image (diamonds) and at a radial distance of 15 mm (triangles; the periphery of the image). (Color figure in online)

3.3 Influence of Temporal and Spatial Laser Beam Properties

3.3.1 Temporal Variations of Laser Power Density

In Subsects. 3.1 and 3.2, a simple, rectangular laser pulse (1) of 1.768×10^{11} W · m^{-2} power density, constant over the target spot (15-mm radius), and of 8 ns duration has been applied to the sample. Whether a different temporal power distribution would affect the results obtained for a_r and a_x has been checked in the following by assuming triangular pulses (2) and (3). Pulse (2) starts at zero power density and linearly increases to a sharp maximum, while pulse (3) starts with a sharp maximum and decreases linearly to zero power density. The power density, $\mathrm{d}Q/\mathrm{d}t$, for the three options is normalized so that the integral over time, $0 \le t \le 8 \times 10^{-9}$ s, and over the total area, A, of the graphite sheet is constant:

$$Q = \int \int (\mathrm{d}Q/\mathrm{d}t)\mathrm{d}t\,\mathrm{d}A = 1\ \mathrm{J} \tag{9}$$

Results for the temperature excursions for pulses (1)–(3) are shown in Fig. 6. Data are given only for node 10 (the central position of the target spot) and node 15 (located at the periphery of the image).

We have seen in Fig. 3a that temperature excursions observed at the "inner" nodes of the set $\{N_x\}$ are already almost identical since these nodes, under a pulse with a homogeneous distribution of power density (as assumed in the simulations), are exposed to

the same irradiation intensity, and the inner nodes experience adiabatic conditions. It is thus sufficient to consider only node 10 in the following. If the intensity changes with time, Fig. 6 of course shows that the temperature increase at this node, similar to the other nodes, in the interval $0 \leq t \leq 8 \times 10^{-9}$ s significantly depends on the temporal structure of the pulse. However, all the curves in Fig. 6 again become identical after the end of the irradiation period. The same applies to the curves calculated for node 15 that is located on the periphery of the image, and it applies, in particular, to those nodes located at positions still more distant from the center, i.e., to the nodes of the set $\{N_r\}$. Saturation of all the curves in Fig. 6 again is at $T = 0.0157$ K over-temperature. This in turn means that the application of Eq. 8 to the temperature excursions obtained for the nodes of set $\{N_r\}$ necessarily yields the *same* radial diffusivity as before, $a_r = 8.085 \times 10^{-4}\,\mathrm{m^2 \cdot s^{-1}}$, for pulses (1)–(3). There is apparently no dependency of the radial diffusivity on the *temporal* structure of the laser pulse, provided data are taken safely outside the image.

Even when extracting the axial component of the diffusivity, results are almost identical to the previous value, $a_x = 3.800 \times 10^{-6}\,\mathrm{m^2 \cdot s^{-1}}$, which was to be expected: All the nodes of the set $\{N_x\}$, are irradiated homogeneously in space; the laser power density varies only with time in this test. There is also apparently no detectable dependence of the axial diffusivity on the *temporal* structure of the laser pulse.

3.3.2 Spatial Variations of Laser Power Density

The same analysis for extraction of a_r and a_x has been performed with three different spatial distributions of the power density. For simplicity, it was assumed that the power density is constant over an image on the front side of the graphite sheet of 5-mm, 10-mm, and (as before) 15 mm radius, with very small contributions outside this area (i.e., within the previous radius of the image of 15 mm). Again, the power density was adjusted to yield the same value ($Q = 1$ J, Eq. 9) after integration over the irradiation period $0 \leq t \leq 8 \times 10^{-9}$ s and the total surface of the graphite sheet. Figure 7 shows strongly differing temperature excursions arising during the irradiation period. The maximum target temperature observed during irradiation and in the period $t \leq 0.1$ ms is about 180 K (over-temperature), which will initiate radiative losses, Q_{Rad}. They can be estimated by division of the total simulated time scale into Sects. 1–3 using

$$Q_{\mathrm{Rad}} = \sigma A_{\mathrm{Target}} (T^4_{\mathrm{Target},1} \Delta t_1 + T^4_{\mathrm{Target},2} \Delta t_2 + T^4_{\mathrm{Target},3} \Delta t_3) \tag{10}$$

σ is the Stefan–Boltzmann constant, A_{Target} is the area of the image of the laser beam impinging onto the front side of the graphite sheet, Δt_1 is the irradiation period (8 ns), Δt_2 is the period (10 ns to 0.1 ms) where the temperature, T_{Target}, is approximately constant (about 160 K, compare Fig. 7), and Δt_3 is the period between 0.1 ms and 0.1 s where T_{Target} decreases approximately linearly to below 1 K. Taking $T_{\mathrm{Target},1} = 180$ K, $T_{\mathrm{Target},2} = 160$ K, and $T_{\mathrm{Target},3} = 0.9 T_{\mathrm{Target},2}$, as a rough average, this yields $Q_{\mathrm{Rad}} < 0.01$ J from the image with 5 mm radius, which can be neglected. Radiation losses from the total surface of the graphite sheet are very small, too, because the sheet will not attain high temperatures during the short period $t \leq \Delta t_3$. The period $t \leq \Delta t_3$ (0.1 s) also is too short to induce convective losses.

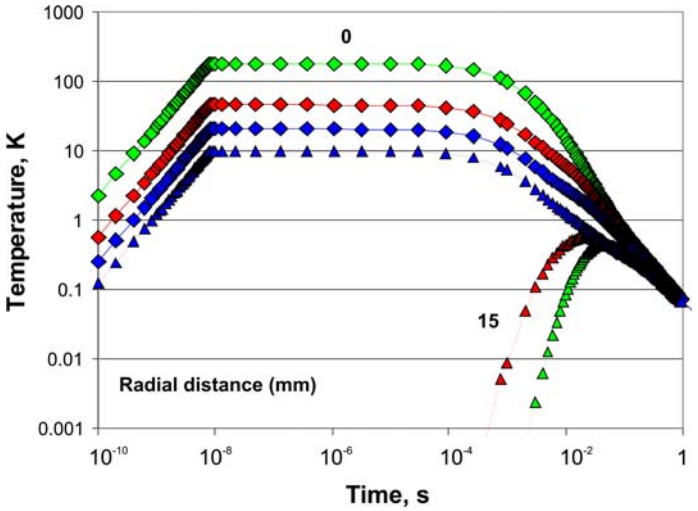

Fig. 7 Numerically simulated, transient node temperatures, $T(t)$, calculated for spatial variations (pulses 1–3) of laser power density impinging on the graphite sheet, with different radii of the images on the front side of the graphite sheet. All the pulses are rectangular (constant in time), duration of the pulses is 8 ns. The radii of images of the pulses 1–3 are 15 mm (blue), 10 mm (red), and 5 mm (green symbols). Data are given at the center of the laser pulse image (diamonds) and at a radial distance of 15 mm (triangles). (Color figure in online)

For extraction of the radial component, it is necessary to increase the distance from the center of the sample to avoid conflicts again with resonance-like oscillations, compare Fig. 8. For a distance of at least 63 mm, the a_r-values converge (without intermediate oscillations) to the values listed in Table 1, again in very good agreement with the input data.

Morevoer, the results obtained for the axial component, a_x, by application of Eqs. 7a, b, depend on the spatial distributions, Eqs. 1–3, of the power density, compare Table 2. The more important the deviations become, the smaller the image radius and the deviations exceed 30 % if the radius is below 5 mm. Whether this situation can be improved, e.g., by application of Eqs. 7a, b to nodes different from the central node has to be clarified in further investigations.

In summary to Subsect. 3.3, while determination of the radial component of the diffusivity apparently is not very sensitive to temporal or spatial variations of the laser power density on the image, the proposed method yet should prefer a homogeneous spatial distribution of the power density in both time and geometry to also yield reliable axial diffusivity components from front-side laser flash experiments.

4 Conclusion

Remote measurement of temperature excursions, and extraction of the anisotropic thermal diffusivity by means of analytical expressions, will be successful if the nodes at which data are taken are properly selected on the basis of the thermal homogene-

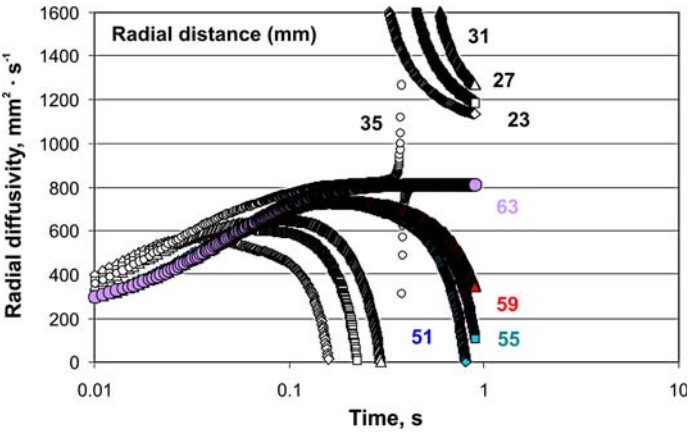

Fig. 8 Radial diffusivity component, a_r, as function of time, t, for a rectangular laser pulse impinging on the front side of the graphite sheet. The image has a radius of 5 mm. Results are given for nodes all located outside the target spot. Open and full symbols (diamonds, rectangles, and triangles) refer to nodes located at radial distances between 23 mm and 35 mm or between 51 mm and 63 mm from the center, respectively. With increasing radial distance, resonance-like oscillations in the component a_r disappear successively (the last oscillation is seen at 35 mm radial distance), and the curves finally converge (constant in time, no more oscillations) to values close to the numerical data input, $a_r = 8.085 \times 10^{-4}\,\mathrm{m^2 \cdot s^{-1}}$

Table 1 Radial diffusivity component, a_r, calculated using Eq. 8; data are obtained using nodes located clearly outside the image radius. Data input to the simulation is $a_r = 8.085 \times 10^{-4}\,\mathrm{m^2 \cdot s^{-1}}$

Image radius (mm)	Radial distance of the node from center (mm)	Radial diffusivity component ($10^{-4}\,\mathrm{m^2 \cdot s^{-1}}$)
15	33.75	8.085
10	63	8.137
5	63	8.136

Table 2 Axial diffusivity component, a_x, calculated using Eq. 7a, b; data are obtained using the central node of the graphite sheet. Data input to the simulation is $a_x = 4.539 \times 10^{-6}\,\mathrm{m^2 \cdot s^{-1}}$

Image radius (mm)	Axial diffusivity component ($10^{-6}\,\mathrm{m^2 \cdot s^{-1}}$)
15	3.800
10	4.936
5	6.030

ity criterion, T_0, and with respect to temporal and spatial structure of the irradiation pulse. The results obtained for a graphite sheet have verified applicability of the method provided an appropriate (fast) Thermo-Vision system is available. Note that the procedure presented so far can be applied reasonably to nearly adiabatic conditions only.

The results can be used for "thermally thin films" when the Biot number, $Bi = \alpha b/\lambda$, is small, e.g., $Bi \leq 0.1$, compare standard literature on heat transfer (α is a heat transfer coefficient). In this case, we have a solely thermal-diffusivity problem. In the present example, the graphite disk of thickness $b = 1$ mm is "thermally" thin but the

method can be applied also to much larger (physical) sample thicknesses, depending on the heat transfer coefficient.

References

1. K.R. Grice, L.H. Inglehart, L.D. Favro, P.K. Kuo, R.L. Thomas, J. Appl. Phys. **54**, 6245 (1983)
2. C. Frétigny, J.P. Roger, V. Reita, D. Fournier, J. Appl. Phys. **102**, 116104 (2007)
3. V. Drach, Aufbau einer 3ω-Apparatur zur Bestimmung der thermischen Eigenschaften von Schichtsystemen, Diploma Thesis, Department of Physics, University of Würzburg, Würzburg, Germany (1992) Report No. E21-0292-1 (1992)
4. J.L. Nzodoum Fotsing, B.K. Bein, J. Pelzl, Superlattice Microst. **35**, 419 (2004)
5. D.G. Cahill, Rev. Sci. Instrum. **61**, 802 (1990)
6. R. Frank, Entwicklung eines Verfahrens zur Messung der anisotropen Wärmeleitfähigkeit in supraleitenden Powder-In-Tube-Bändern, Doctoral thesis, Department of Physics, University of Würzburg, Würzburg, Germany (1995)
7. E.T. Swartz, Doctoral thesis, Faculty of the Graduate School of Cornell University, Materials Science Center, Cornell University, Ithaca, NY (1987)
8. Y. Taguchi, Y. Nagasaka, Int. J. Thermophys. **22**, 289 (2001)
9. O.Yu. Troitsky, H. Reiss, High Temps.—High Press. **32**, 391 (2000)
10. O.Yu. Troitsky, H. Reiss, High Temps.—High Press. **35/36**, 265 (2003/2004)
11. O.Yu. Troitsky, H. Reiss, Int. J. Thermophys. **28**, 1536 (2007)
12. H.S. Carslaw, J.C. Jaeger, *Conduction of Heat in Solids*, 2nd edn. (Clarendon Press, Oxford, 1959)
13. I.G. Kozhevnikov, L.A. Novitsky, *Teplofizicheskiye svoistva materialov pri nizkikh temperaturakh: Spravochnik, Thermophysical Properties of Materials Under Low Temperatures: Handbook* (Mashinostroyeniye, Moscow, 1982), p. 382
14. P. Cielo, J. Appl. Phys. **56**, 230 (1984)
15. *ThermoVision SC6000 HS*, FLIR Systems AB, Danderyd, Sweden